

# Light chaotic dynamics in the transformation from curved to flat surfaces

Chenni Xu<sup>1,2</sup>, Itzhack Dana<sup>1</sup>, Li-Gang Wang<sup>2</sup>, and Patrick Sebbah<sup>1\*</sup>

<sup>1</sup> *Department of Physics, The Jack and Pearl Resnick Institute for Advanced Technology, Bar-Ilan University, Ramat-Gan 5290002, Israel and*

<sup>2</sup> *Zhejiang Province Key Laboratory of Quantum Technology and Device, Department of Physics, Zhejiang University, Hangzhou, 310027, Zhejiang, China*

Light propagation on a two-dimensional curved surface embedded in a three-dimensional space has attracted increasing attention as an analog model of four-dimensional curved spacetime in laboratory. Despite recent developments in modern cosmology on the dynamics and evolution of the universe, investigation of nonlinear dynamics of light in non-Euclidean geometry is still scarce and remains challenging. Here, we study classical and wave chaotic dynamics on a family of surfaces of revolution by considering its equivalent conformally transformed flat billiard, with nonuniform distribution of refractive index. This equivalence is established by showing how these two systems have the same equations and the same dynamics. By exploring the Poincaré surface of section, the Lyapunov exponent and the statistics of eigenmodes and eigenfrequency spectrum in the transformed inhomogeneous table billiard, we find that the degree of chaos is fully controlled by a single geometric parameter of the curved surface. A simple interpretation of our findings in transformed billiards, the “fictitious force”, allows to extend our prediction to other class of curved surfaces. This powerful analogy between two a priori unrelated systems not only brings forward a novel approach to control the degree of chaos, but also provides potentialities for further studies and applications in various fields, such as billiards design, optical fibers, or laser microcavities.

## I. INTRODUCTION

Einstein’s general theory of relativity (GR) unprecedentedly interprets gravity in a geometrical framework, namely, the presence of a massive object distorts the very fabric of the space and time in its vicinity. Despite of GR’s triumph, gravitational effects are in principle too feeble for light to be perceived in laboratory environment. One of the analog models of GR is two-dimensional (2D) curved surfaces embedded in 3D space, whose theoretical cornerstones are the 3+1 membrane paradigm [1] and embedding diagrams. After taking a constant time and extracting the equatorial slice of a spherically symmetrical space, the remnant metric can be visualized through a 2D curved surface. Ever since this innovative notion was brought up by Batz and Peschel [2], electromagnetic (EM) dynamics and wave propagation on 2D curved surfaces have been prosperously developed both theoretically [3–10] and experimentally [11–15]. On the other hand, GR notions could reciprocally contribute to the engineering of nanophotonic devices [15, 16] and transformation optical designs, ranging from EM invisible cloaks [17, 18] to perfectly focusing lens [19–21], based on manipulation of the curved geodesic paths.

Investigation of nonlinear dynamics in the context of GR may date back to 1960s, and has been extensively discussed in various aspects [22–24]. Nonlinear dynamics, or chaos, widely exists in diverse modern scientific disciplines. One characteristic of chaos is the exponential sensitivity to initial conditions, with a well-publicized metaphor being the “butterfly effect”. In the recent

decades, instead of being considered a nuisance, wave chaos has been taken advantage of to ameliorate optical resonators and laser microcavities [25–34], such as enhancing energy storage [25], suppressing spatiotemporal lasing instabilities [26], realizing high power directional emission [27–29], etc. To this end, information about dynamical behaviors in 2D cavity, such as critical periodic orbits and volume of chaotic area in phase space, is significant. One paradigm model is a 2D table (or flat) billiard, which is typically a closed domain wherein particles and light rays propagate freely, except for elastic collisions on its boundaries. Various degrees of chaos in table billiards are realized by either deforming the boundaries [35–37] or introducing external force [38–40]. In a recent work, a novel notion, transformed cavity, is proposed with a nonuniform profile of refractive index present in a deformed optical cavity [41]. Such transformed cavity opens up a new pathway of chaos engineering.

Investigation of light chaotic dynamics in a non-Euclidean geometry remains challenging from the complexity of the equations induced by the curved geometry, as well as the ambiguity of concepts, such as the definition of boundaries and indicators of chaos. To the best of our knowledge, the wave chaos idea has been carried over in a few curved elastic systems [42–44], such as aluminum thin shells [42], yet has rarely been explored in optics, except for a very recent study about ray chaotic behavior on a deformed toroidal surface [45]. Here we address this challenge by developing the analogy between a curved surface and a 2D table billiard with nonuniform distribution of refractive index, on the strength of transformation optics (TO). The mathematical underpinning of TO is the form invariance of Maxwell equations under general coordinate transformation, with the optical constitutive parameters of the transformed media (i.e.,

---

\*patrick.sebbah@biu.ac.il

engineering the permittivity  $\varepsilon$  and permeability  $\mu$  tensor explicitly) [46, 47]. As we will demonstrate, this approach of projection provides a possibility to utilize physical systems on one surface to explore their counterparts on the other, especially when the studies in one of the systems are demanding to carry on.

In this work, we study classical and wave chaos on a special type of 2D curved surfaces in 3D space, surfaces of revolution (SORs), by investigating light propagation in its corresponding table billiard with azimuthally symmetric nonuniform distribution of refractive index. We exemplarily choose a typical family of SORs, the Tannery's pears. Since such surfaces are integrable, we consider half of the pear and its 2D nonuniform billiard where a circular hole is pierced to introduce chaos. We first establish that these two systems share the same dynamics by showing that a conformal coordinate transformation preserves both geodesic equations and wave equations. Thanks to this equivalence, we can assess the degree of chaos in one system (the curved surface) by probing the nature of the trajectories in Poincaré surface of section (SOS) and measuring the Lyapunov exponent in the other (the flat billiard). We find that the degree of chaos is fully controlled by a single geometrical parameter of the Tannery's pear. This is also revealed in the statistics of eigenmodes of the Tannery's pears, as the wave equation is invariant for both systems. At last, we show that the above results can be generalized to arbitrary SORs, by coming up with a universal quantity in the 2D nonuniform billiards. This simple interpretation further demonstrates the potentialities of our approach.

## II. RESULTS

### Basic theory

As its name indicates, a SOR can be generated by revolving an arbitrary plane curve (known as generatrix) around an axis of symmetry for a circle. The line element of a typical SOR takes the form  $ds^2 = g_{\alpha\beta}dx^\alpha dx^\beta = E(u)du^2 + G(u)dv^2$ , with  $u$  along longitudinal direction and  $v$ , being the rotational angle, along transverse direction, as shown in Fig. 1A. In curved spaces, light rays propagate along geodesics, in analogy with straight lines in free space. On the basis of geodesic equations, an arbitrary geodesic with given initial conditions is depicted by (for mathematical details, see SI Appendix, section 1)

$$dv = \eta \frac{\kappa \sqrt{E(u)}}{G(u) \sqrt{1 - \frac{\kappa^2}{G(u)}}} du. \quad (1)$$

Here  $\eta = \text{sgn}[(du/ds)_{\text{initial}}]$  is determined by the initial direction, and slant  $\kappa$ , defined as  $[G(u)dv/ds]_{\text{initial}}$ , remains invariant as a consequence of the conservation of angular momentum [9]. When it comes to waves, the time-harmonic scalar EM field follows the massless Klein-

Gordon equation

$$\frac{1}{\sqrt{E(u)G(u)}} \frac{\partial}{\partial u} \left[ \sqrt{\frac{G(u)}{E(u)}} \frac{\partial \Phi}{\partial u} \right] + \frac{1}{G(u)} \frac{\partial^2 \Phi}{\partial v^2} + k^2 \Phi = 0, \quad (2)$$

with  $k$  being the propagation constant [48].

In this work, instead of directly investigating light propagation on the surface, we employ an innovative method by projecting a SOR onto a plane with distribution of refractive index, in light of conformal transformation optics [49, 50]. This notion is mathematically underlain by the theorem that any 2D Riemannian manifold is conformally flat. Namely, the metric of an arbitrary 2D curved surface  $ds^2$  can be conformally related to the metric of a flat plane  $ds_f^2$  through  $ds^2 = \Lambda ds_f^2$ , where  $\Lambda$  is a differentiable function [51]. Interestingly, the right-hand side, defined as  $ds'^2$ , perfectly describes an inhomogeneous planar dielectric medium with spatially varying refractive index  $n' = \sqrt{\Lambda}$ . For SORs, thanks to their rotational symmetry, we can naturally suppose the projected plane is azimuthally symmetric. Consequently, polar coordinate is chosen out of convenience and the variation of refractive index rests exclusively on radial component. Based on the premise that  $ds^2 = ds'^2$ , an equivalence between these two systems can be established through the coordinate mapping

$$r(u) = A \exp \left[ \int^u \sqrt{\frac{E(u')}{G(u')}} du' \right], \quad v = \varphi, \quad (3)$$

with distribution of refractive index

$$n'(u) = \frac{\sqrt{G(u)}}{A} \exp \left[ - \int^u \sqrt{\frac{E(u')}{G(u')}} du' \right]. \quad (4)$$

Here  $A$  is a positive integration constant,  $r$  and  $\varphi$  are radial and azimuthal coordinates, respectively.

By virtue of this coordinate mapping, transformed version of Eq. (1) appears as

$$d\varphi = \eta' \frac{\kappa'}{n'(r)r^2 \sqrt{1 - \frac{\kappa'^2}{n'^2(r)r^2}}} dr, \quad (5)$$

with  $\eta' = \text{sgn}[(dr/ds')_{\text{initial}}]$  and  $\kappa' = [n'^2(r)r^2 d\varphi/ds']_{\text{initial}}$ . We prove in SI Appendix 2 that Eq. (5) is the very solution of geodesic equations on the projected plane. Thus the dynamics of light rays are preserved in both systems. In terms of waves, Eq. (2) is transformed into

$$\frac{1}{r} \frac{\partial}{\partial r} \left( r \frac{\partial \Phi}{\partial r} \right) + \frac{1}{r^2} \frac{\partial^2 \Phi}{\partial \varphi^2} + k^2 n'^2(r) \Phi = 0, \quad (6)$$

which is exactly the wave equation of electric field on a plane with distribution of azimuthally symmetric refractive index  $n'(r)$ . As a result, the transformation preserves the solutions of wave equation in one system to

be the eigenmodes of another. In SI Appendix 2, we extend this result to arbitrary curved surfaces, demonstrating the universality of the transformability of both geodesic equations and wave equations. We have shown, therefore, that the dynamical properties of both optical rays and waves are absolutely identical on a homogeneous SOR and on its transformed inhomogeneous plane, and we can safely investigate one system to infer about the other.

When a SOR is closed (e.g. sphere, spindle) or infinitely extends (e.g. cylinder, cone), its projection covers the whole plane. A paradigmatic example is the so-called “Tannery’s pear”, which is an object of interest for mathematicians [52] and is going to be the study case of this paper. The family of Tannery’s pears can be parametrized by  $E(u) = (c + \cos u)^2$ ,  $G(u) = \sin^2 u$ , with  $c$  being a positive constant and in the meantime, the single parameter to describe this family of surfaces. It is proved that such surfaces have a constant period function  $2c\pi$  [53]. That is, when the parameter  $c$  is an integer, all the geodesics (except the ones along longitudinal  $u$  direction) are closed, and for a particle which departs from an arbitrary position on the geodesic, moves along it and returns to the starting point, the accumulated variation in coordinate  $v$  is  $2c\pi$ , as shown in Fig. 1B. In order to limit our study to a finite area on plane, a mirror is put on the “equator” (i.e., the latitude with  $u = \pi/2$ , see the black dashed lines in Figs. 1C and 1D) of the surface, which plays the role of a perfectly reflecting boundary, and only the lower half of surface is taken. On the projected plane, the equator corresponds to a circle with unit radius, while the lower half of surface corresponds to the area inside the circle, which together naturally form a circular billiard, as shown in the right column of Figs. 1C and 1D. These two systems are absolutely integrable, since the number of constants of motion (energy and orbital angular momentum) equals to the dimensionality of the system [54], owing to the rotational symmetry of SORs. To introduce chaos in this system, an off-centered disk-shaped area is eliminated, leaving a circular hole with a specular boundary in the billiard. The choice of a disk shape is out of consideration of simpleness, yet more complex shapes could be explored. The right column of Figs. 1C and 1D shows two typical holes whose centers are located at 0.2 (in unit of radius) from the centers of the billiards, and whose radius are 0.3 and 0.1, denoted by dark green and orange dotted lines, respectively. By taking the coordinate transformation Eq. (3), the correspondence of these two holes on the surface are shown in the left column. It is seen that the refractive index approaches to infinity at the center of the projected billiard, corresponding to the apex of the surface in the bottom, which is basically a singularity for light rays. We focus in the rest of the paper on the cases where the hole includes the billiard center, resulting in the removal of the bottom apex. Its correspondence on the surface is a boundary unparallel to latitudes, rather than a hole.

In what follows, in order to distinguish them from their

2D projected billiards, SORs are referred to as “3D surfaces”, based on the fact that they are embedded in 3D space in spite of being 2D per se.

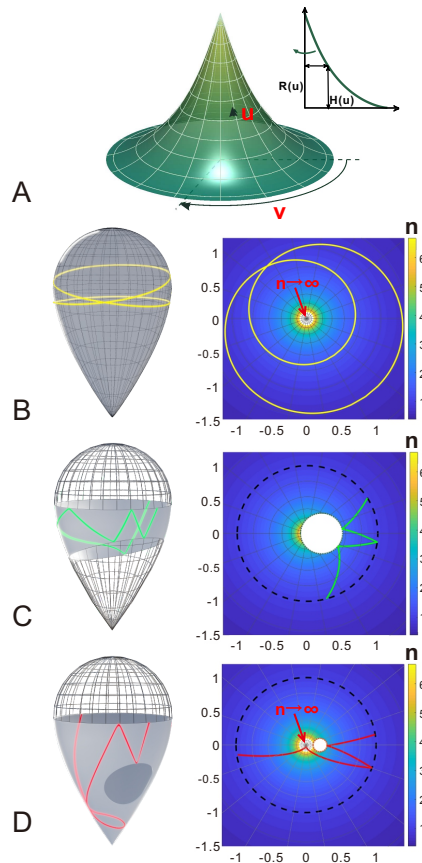


FIG. 1: (A) Sketch of a typical SOR with the orthogonal curvilinear coordinates on it. The inset illustrates its generatrix. (B) Tannery’s pear with  $c = 2$  (left) and its projected billiard (right). A typical closed trajectory is depicted by yellow solid line. (C),(D) Truncated Tannery’s pears which have a circular hole with (C) radius 0.3 (dark green dotted line) and (D) radius 0.1 (orange dotted line) in their projected billiards. The equators are denoted by black dashed lines in the projected billiards. Two typical trajectories are plotted by green and red solid lines, respectively.

### Poincaré surface of section

Ray trajectories become rapidly intractable in real space after few bounces, it is therefore more advisable to inspect ray motions in phase space which are composed of two spatial dimensions and their conjugate momenta. For billiard systems, an effective approach to extract information from 4D phase space is to record the states of the trajectory exclusively when it collides on the outer boundary. This 2D section of phase space is known as Poincaré surface of section (SOS), and is conveniently depicted in the framework of Birkhoff coordinate,

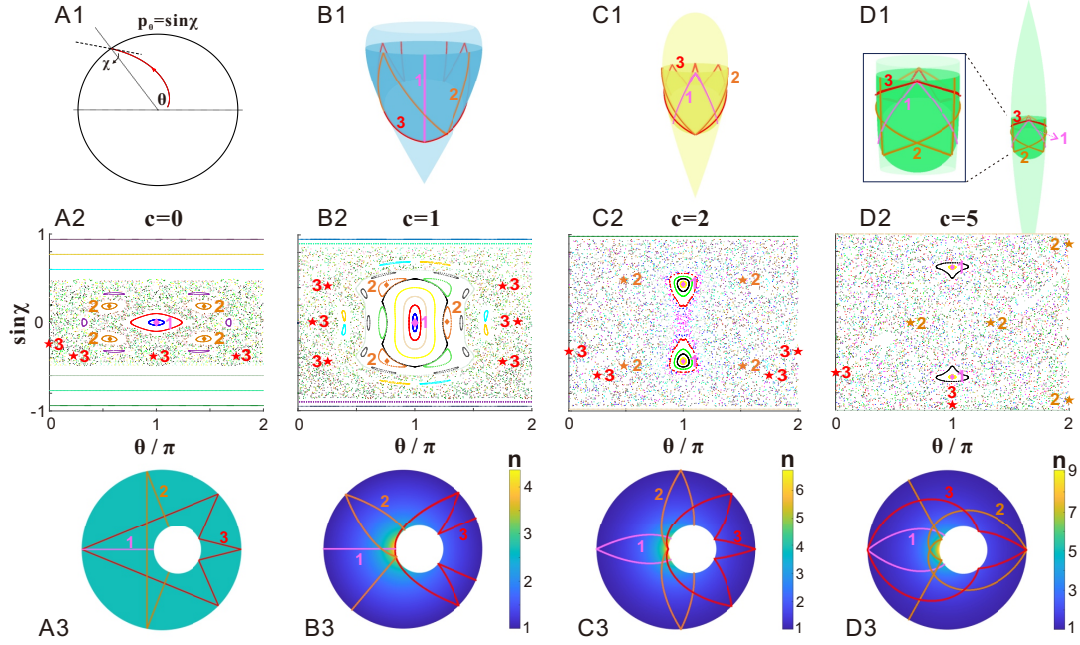


FIG. 2: Poincaré surfaces of section of Tannery's pears with different parameter  $c$ . (A1) Sketch of Birkhoff coordinates. (B1),(C1),(D1) Sketches of Tannery's pears with  $c = 1, 2$  and  $5$ , respectively. The transparent parts correspond to areas outside the projected billiard and inside the hole, which are excluded in the study. (A2),(B2),(C2),(D2) Poincaré surface of section of Tannery's pears with  $c = 0, 1, 2$  and  $5$ , respectively. Each color represents an arbitrary trajectory. The diamonds and pentagrams respectively indicate typical stable and unstable periodic orbits, whose representations in Poincaré surface of section are a succession of points. These periodic orbits in real space are exhibited in (A3), (B3), (C3), (D3), respectively, corresponding to the points with the same label and color.

as sketched in Fig. 2A1. In practice, the trajectories between two bounces are traced by Eq. (1). When the trajectories collide on the hole/lower unparallel boundary, the rule of specular reflection is applied in the 2D projected billiard, after projecting the trajectories on 3D surface back to the inhomogeneous plane. This step saves one from complicated or even impracticable calculation on 3D surface, since the analytical expression of the lower unparallel boundary is inaccessible.

When  $|\sin \chi|$  is large enough, trajectories propagate near the outer boundary of 2D projected billiard/equator of 3D surface and are therefore free from colliding on the hole/lower unparallel boundary. Their tangential momenta  $|\sin \chi|$  remain invariant, so that in Poincaré SOS these trajectories are represented by horizontal straight lines. In contrast, trajectories with small  $|\sin \chi|$  collide on the hole/lower unparallel boundary, resulting in their representations ergodically and irregularly distributed in the central part of Poincaré SOS, which therefore forms a chaotic sea. Among these trajectories, some return to their initial conditions after several bounces, and retrace themselves repeatedly. Such periodic orbits (POs) are represented as a succession of points in SOS, with the number of points equal to the number of bounces on the outer boundary/equator in each period. For some POs, the trajectories whose initial conditions are slightly deviated from the critical conditions of POs are able to sur-

vive in the vicinity of the latter. Such POs, considered as stable POs, form regular islands among the chaotic sea in Poincaré SOS together with their quasi-periodic orbits. As a contrast, the other unstable POs are submerged in the chaotic sea and can be scarcely recognized. Some typical stable and unstable POs are illustrated by diamonds and pentagrams respectively in the middle row of Fig. 2, and the corresponding trajectories in the billiards are depicted in the last row with same labels and colors. An interesting feature of PO with label 1 is explicated in SI index, section 3.

A generic presentation about the Poincaré SOSs of four typical Tannery's pears with  $c = 0, 1, 2, 5$  is given in Fig. 2. Different shapes of the surfaces are clearly exhibited in Figs. 2B1, 2C1 and 2D1. Specially, when  $c = 0$ , the metric of the surface degenerates to  $ds^2 = \cos^2 u du^2 + \sin^2 u dv^2$ , which is equivalent to a polar coordinate if one takes  $\sin u$  as the radial component and  $v$  as the azimuthal component. Thus, surface with  $c = 0$  corresponds to the flat billiard and serves as reference. The Poincaré SOSs reveal that the phase spaces of all the four surfaces are mixed, with coexistence of both regular and chaotic trajectories. One can observe that the area of chaotic sea remarkably enlarges with the parameter  $c$ , implying an increasingly chaotic phase space structure of Tannery's pear with greater parameter  $c$ . Another phenomenon one may meanwhile notice is an

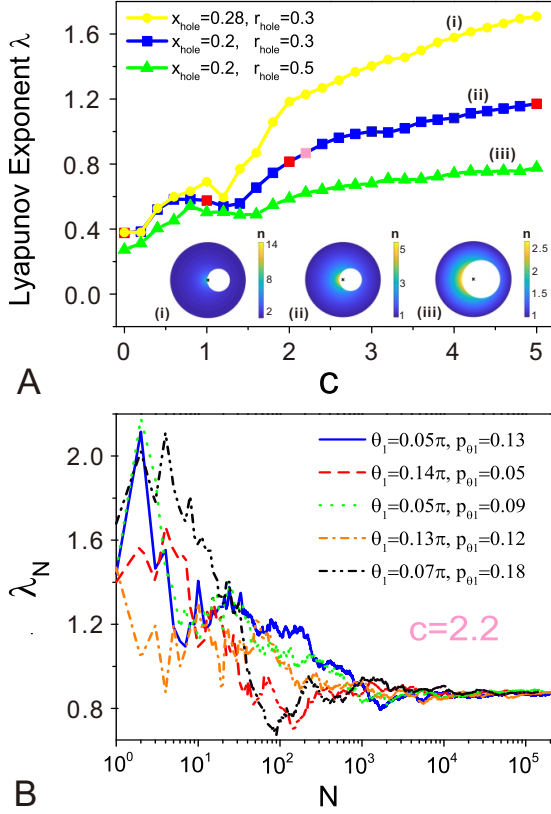


FIG. 3: (A) Variation of Lyapunov exponents versus the parameter  $c$  of Tannery’s pears and three different means of truncation. The distribution of refractive index are illustrated in the inset with corresponding labels, and the black cross denotes the center of the billiard. The red square data markers in line (ii) correspond to the cases illustrated in Fig. 2. (B) The quantity  $\lambda_N$  at  $N$ th bounce, calculated by Eq. (7). Five pairs of extremely close trajectories are randomly chosen at the case denoted by the pink square data marker in (A), whose initial conditions are shown in the legend with  $\theta_2 = \theta_1 + 10^{-4}$ ,  $p_{\theta_2} = p_{\theta_1} + 10^{-4}$ . All the five pairs of trajectories converge to the same asymptotic value, which is defined as Lyapunov exponent.

obvious reduce in the amount of stable POs and the area of islands, especially in Figs. 2B2, 2C2 and 2D2. These two hints suggest an increasing proportion of trajectories transferring from regular to chaotic, and consequently indicate a more significant degree of chaos. Note that this observation is true both on 3D surface and in 2D billiard with refractive index landscape, because of their equivalence.

### Lyapunov exponent

As was mentioned, a hallmark of chaos is the sensitivity to initial conditions, i.e., the exponential divergence of two extremely nearby trajectories in phase space. The speed of this exponential divergence is characterized by

the (maximum) Lyapunov exponent  $\lambda$ . Here, we adopt the method of “billiard map” in terms of the collisions of trajectories on the outer boundary, instead of the “billiard flow” with continuous time [55]. In this way, Lyapunov exponent is defined as

$$\lambda = \lim_{N \rightarrow \infty} \frac{1}{N} \sum_{i=1}^N \ln \frac{|\delta_i|}{|\delta_0|}, \quad (7)$$

where  $|\delta_i|$  is the distance of the two chosen trajectories in phase space at the  $i$ th bounce. In practice, two sets of extremely close initial conditions are randomly chosen from the chaotic area in Poincaré SOS, and distance  $|\delta|$  is collected everytime two trajectories collide on the outer boundary. Theoretically, if the number of bounces  $N$  is large enough, Eq. (7) is supposed to approach to a constant which is independent of the choice of initial conditions. Technical details about the calculation of Lyapunov exponents are specified in SI index, section 4.

By this method, Lyapunov exponents of a series of Tannery’s pears with varying parameter  $c$  and under three different means of truncation are calculated and illustrated in Fig. 3A. Each data point in Fig. 3A is the result of averaging over 4-6 randomly-chosen pairs of trajectories, where each pair of trajectories experiences several tens of thousands of bounces on the outer boundary/equator, and an approximate convergence has been reached (Example of five typical pairs of trajectories is shown in Fig. 3B). The figure manifests an overall increasing tendency of Lyapunov exponents with increasing parameter  $c$  of Tannery’s pears, indicating that in general, when parameter  $c$  increases, the speed of divergence between two close trajectories, or the instability of the trajectories increases, which validates the increase of degree of chaos both on the 3D surface and in the 2D projected billiard. Furthermore, the invariance of this increasing tendency in spite of different positions and radii of the pierced hole in the projected billiard attests the universality of this feature, as shown in Fig. 3A. Compared with the qualitative interpretation obtained from Poincaré SOS with a coarse sampling of parameter  $c$ , this signature brings a more quantitative insight, which enables a finer exploration and hence reveals more details about the dependence of chaoticity on parameter  $c$ . One example is that an exception to this increasing trend is observed near  $c = 1$ , elucidating that the variation of chaoticity with parameter  $c$  is not strictly monotonous.

### Statistics of eigenmodes and eigenfrequency spectrum

When it comes to quantum or wave realm, notions of phase space and trajectories are not properly defined due to the uncertainty principle. Therefore, signatures in classical chaos are no longer valid, but are replaced by quantum mechanical criteria based on energy spectrum, energy eigenvectors, entanglement, temporal evolution of



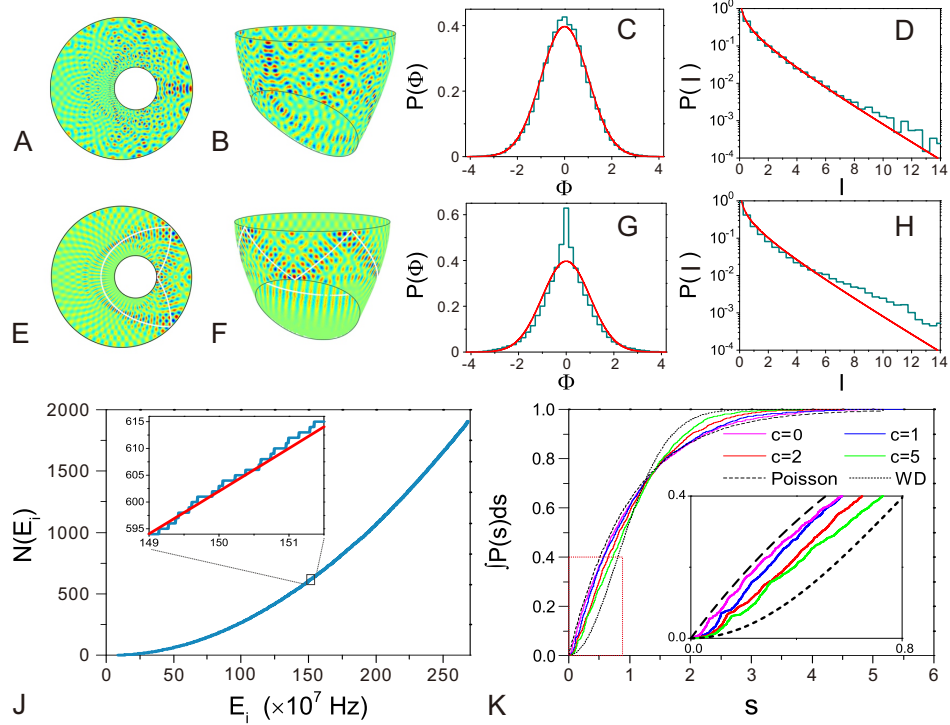


FIG. 4: (A)-(H) Spatial statistics of eigenmodes. (A),(B) The field distributions (amplitude) of a typical ergodic eigenmode (frequency  $\omega = 2.9639$  GHz) of truncated Tannery's pear with  $c = 1$  in projected billiard (A) and on 3D surface (B). Its distribution of amplitude and intensity are plotted in (C) and (D), respectively, with red solid line being Gaussian and Porter-Thomas distribution as reference. The field distributions (amplitude) of a typical scarring eigenmode (frequency  $\omega = 2.8863$  GHz) and their statistics are shown in (E)-(H). The white solid lines in (E) and (F) indicate its corresponding unstable periodic orbit. (J),(K) Statistics of eigenfrequency spectrum. (J) Cumulative eigenfrequency density  $N(E_i)$  of Tannery's pear with  $c = 2$  versus eigenfrequency  $\{E_i\}$ . (K) Distribution of nearest neighbor spacing of Tannery's pears with  $c = 0$  (purple), 1 (blue), 2 (red) and 5 (green). The Poisson (black dashed) and Wigner-Dyson (black short dashed) distribution are also plotted as reference. (Inset) Zoom-in of the area marked by red dotted rectangle.

expectation values, etc. In this section, we are going to focus on the first two fingerprints.

We have demonstrated that the wave equation on a SOR is identical with that in its projected billiard, bridged by the coordinate transformation. Namely, the performed calculation as well as the concepts and phenomena in one system can be automatically extended to the other. Here, we obtain eigenmodes in both systems with the help of COMSOL Multiphysics 5.2. In practice, the simulation is conducted in the 2D inhomogeneous billiard, because of the difficulty in constructing 3D surface (especially when the expression of the lower unparallel boundary is unknown), and the eigenfunction on 3D surface is subsequently obtained by projection from 2D billiard via the coordinate transformation. Three typical eigenmodes in both systems are illustrated in SI index, Fig. S4.

One credible imprint of ray chaos resides in the spatial statistics of eigenmodes [56]. To be specific, the wave function of a typical ergodic eigenmode, whose classical correspondence has a stochastic motion, distributes uniformly over the whole available area of the phase space which is ergodically visited by its classical trajectories.

Such modes are thus conjectured as a random superposition of plane waves with different amplitudes, phases and directions but same wavenumber, manifesting an analogous pattern of laser speckles. As per central limit theorem, such field is Gaussian random, implying the amplitude of eigenmode follows the Gaussian statistical distribution

$$P(\Phi) = \frac{1}{\sqrt{2\pi\langle\Phi\rangle}} \exp\left(-\frac{\Phi^2}{2\langle\Phi\rangle}\right), \quad (8)$$

while the probability distribution of intensity  $I = \Phi^2$  is subjected to

$$P(I) = \frac{1}{\sqrt{2\pi I/\langle I\rangle}} \exp\left(-\frac{I}{2\langle I\rangle}\right), \quad (9)$$

known as Porter-Thomas (PT) distribution. Figs. 4A and 4B illustrate a typical ergodic eigenmode of truncated Tannery's pear with  $c = 1$ , both on 3D surface and 2D projected plane. The good agreement of its  $P(\Phi)$  and  $P(I)$  with Gaussian and PT distribution respectively validates the ergodicity of the eigenmode.

Besides ergodic modes with speckle statistics, there exists a special class of modes with enhanced amplitude in the vicinity of single unstable periodic orbits in the corresponding classical system. This ubiquitous yet remarkable phenomenon is well known as Quantum Scarring [57]. Unlike the enhancement of eigenstate intensity near stable periodic orbits which are well understood by semiclassical theory of integrable systems, scar was initially an unexpected phenomenon and later found to be a significant correction to predictions from random matrix theory and Gutzwiller trace formula. One of scarred modes of truncated Tannery's pear with  $c = 1$  on projected plane and 3D surface is exhibited in Figs. 4E and 4F, superimposed by a white solid line indicating its corresponding unstable periodic orbit. A prominent deviation of  $P(\Phi)$  and  $P(I)$  from ergodicity can be clearly observed in Figs. 4G and 4H respectively.

Another classic and widely recognized indicator for the randomness of a quantum system is the distribution of nearest neighbor spacing (NNS) of eigenfrequency spectrum [58]. In a classically integrable system, successive eigenfrequency distributes randomly, and the NNS  $s$  follows the Poisson law

$$P_{\text{Poisson}}(s) = \exp(-s), \quad (10)$$

with its peak located at zero. While in classically chaotic systems, the presence of level repulsion leads NNS to best fit Wigner-Dyson (WD) distribution

$$P_{\text{WD}}(s) = \frac{\pi s}{2} \exp\left(-\frac{\pi}{4}s^2\right). \quad (11)$$

Contrast with Poisson distribution where level spacing can be zero with highest probability, a salient consequence of level repulsion is the vanishment of infinitesimal NNS, i.e.,  $P(s) \rightarrow 0$  when  $s \rightarrow 0$ . This behavior can be well explained by the Bohigas-Giannoni-Schmit conjecture [59] that spectra of time-reversal-invariant systems reveal the same fluctuation properties as a Gaussian orthogonal ensemble in random matrix theory. When the system has mixed dynamics, its distribution of NNS is intermediate between the two limiting cases. In virtue of COMSOL Multiphysics 5.2, we got access to the eigenfrequency spectra and consequently performed an unfolding procedure (For more details, see SI index, section 5). The resulting distributions of NNS of truncated Tannery's pears with  $c = 0, 1, 2, 5$  are plotted in Fig. 4K. In order to eliminate the effect of artificially-chosen interval on the distribution curve, we adopt the cumulative distribution instead of widely-used histogrammic representation. One can clearly observe that distributions of NNS of all the four cases interpolate between Poisson and WD distributions, indicating that these surfaces are mixing systems. Comparing the distributions of the four cases, especially in the range of small spacing  $s$  which is zoomed in in the inset, the distribution curve gradually deviates from Poisson distribution and inclines to WD distribution with the increase of parameter  $c$ , manifesting a tendency of increasing chaoticity.

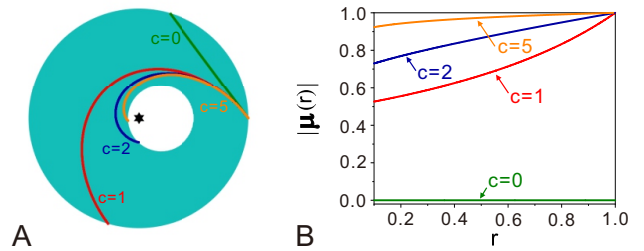


FIG. 5: “Fictitious force” in projected billiards of Tannery’s pears with different  $c$ . (A) Comparison of trajectories with same initial conditions,  $\theta = 0$  and  $p_\theta = 0.8$ , in projected billiards of Tannery’s pears with  $c = 0$  (green), 1 (red), 2 (blue) and 5 (orange). The star marks the position of the center of billiard. (b) Comparison of the four surfaces on  $|\mu(r)|$ , the quantity defined to characterize the degree of trajectories’ deflection.

### III. DISCUSSION

The above-mentioned three signatures explicitly demonstrate an increasing tendency of chaoticity with the geometrical parameter  $c$ . In this section we propose a qualitative interpretation on this phenomenon. One should note that it is the unparallel lower boundary on the 3D surface/hole in the projected billiard, or namely, the breaking of symmetry that gives birth to the chaotic dynamics in the first place [60]. On this basis, the presence of curved surface further alters the chaoticity. There are two parallel approaches to conduct the analysis, either on 3D surfaces or in 2D projected billiards. When considering from the perspective of 3D surfaces, on different SORs trajectories follow their respective geodesics, the undisturbed natural paths. Yet the lower unparallel boundaries, which are the reciprocal projection of the hole in the projected billiards, have different shapes, leading to different degrees of chaos. However, the various properties of surfaces, such as the expression of generatrix, curvature, etc, could perplex the discussion. Whereas, after being projected onto a plane, all the information relevant to chaotic dynamics is completely and merely embodied in the distribution of reflective index (since the location and radius of the hole are fixed in all projected billiards with varying  $c$ ), which simplifies the problem to a great extent. Fig. 5A compares trajectories with identical initial conditions in the projected billiards of Tannery’s pears with parameter  $c = 0, 1, 2, 5$ . One can observe visually that with the presence of nonuniform refractive index, the trajectories deflect towards the center of the billiard, as if they were subjected to a “fictitious force”. More importantly, in the projected billiard with greater parameter  $c$ , the trajectories experience more conspicuous deflections, enhancing the chance of collision on the hole. Put in another way, a greater initial tangential momentum  $p_\theta$  is required to realize the whispering gallery orbits, resulting in a larger area of chaotic sea and consequently a greater chaoticity

of the system. We surmise that the degree of deflection is proportional to the rate of variation of refractive index, and hypothetically quantify the “fictitious force” to be

$$\boldsymbol{\mu} = \frac{r}{n(r)} \nabla n(r), \quad (12)$$

with  $r$  being the radial coordinate, and  $n(r)$  being refractive index profile. Details about construction of Eq. (12) are revealed in SI index, section 6. Owing to the azimuthal symmetry of SORs,  $\boldsymbol{\mu}$  is along the radial direction. Further calculation shows that the magnitude of  $\boldsymbol{\mu}$  is determined uniquely by the metric of the surface (see SI index, section 7). Besides, one may observe that the term in the absolute value sign is always negative, indicating that in the projected billiards of any SORs, the “fictitious force” always points towards the center of billiard. Fig. 5B illustrates the increasing trend of  $|\boldsymbol{\mu}(r)|$  with parameter  $c$ , which coincides with our assumption. Our interpretation is supported by Fig. 3A, which shows the dependence of the Lyapunov exponent with parameter  $c$  for 3 different positions and diameters of the hole. The difference between these three curves is a direct consequence of both the pierced hole and presence of refractive index. Indeed, when the hole is moved away from the center of billiard, or its size reduces, the billiard is farther from being symmetric, leading to a higher degree of chaos. In the meantime, areas with higher refractive index are free from being eliminated and are revealed, further amplifying this difference.

We further inspect the general applicability of quantity  $|\boldsymbol{\mu}(r)|$  in SI index, section 7, by exploring some other typical SORs and comparing their  $|\boldsymbol{\mu}(r)|$ s with the volume of chaotic area in their Poincaré SOSs. The results confirm the universality of  $|\boldsymbol{\mu}(r)|$ . When the studied objects are generalized from Tannery’s pears to general SORs, different SORs are parameterized by different parameters, and even for SORs which are from a same family, the relation between their parameters and the degree of chaos might not be as simple as it is in Tannery’s pears: that is where a universal quantity could play a significant role. Another remarkable advantage of defining  $|\boldsymbol{\mu}(r)|$  is that given a SOR, one is able to approximately estimate its degree of chaos by simply calculating its  $|\boldsymbol{\mu}(r)|$ , which can be directly obtained by its metric, instead of investigating more involved signatures of chaos, as we did earlier.

#### IV. CONCLUSION

In conclusion, we have investigated photonic chaotic dynamics (ray and wave behaviors) on both 3D uniform SORs and in 2D table billiards with nonuniform refractive index. By applying a conformal coordinate transformation, these two systems are proved to be essentially equivalent for both light rays and waves. This complete equivalence enables these two different systems to share interesting phenomena and serve one another to solve in a simpler manner a complex problem, since a geometry

can appear easy and analytical in one system, but untraceable in the other. The present proposal, projecting a 3D SOR into a nonuniform table billiard, serves as an innovative pathway to help both solve calculation and simulation problems and provide with a natural interpretation of the role of curvature in 3D chaotic systems, which probably could be done on the 3D SOR as well but are much simpler and more straightforward to investigate in the latter. Compared with 3D surfaces, a nonuniform 2D table billiard turns out to be a more promising candidate for experimental design and realization, on account of the difficulty in restricting and controlling lights on the former. Reciprocally, the landscape of refractive index in nonuniform table billiards can be complex, while transferring it to its corresponding 3D SOR could greatly reduce the parameters. Our investigation also raises an interesting proposal on the design of refractive index in a nonuniform billiard or cavity to achieve expected features, taking advantage of special trajectories or geometrical properties of its corresponding 3D surface. For instance, it is still an open question for how to transfer an arbitrarily deformed chaotic billiard into integrable, by correlating its refractive index profile with a SOR. More underlying physics and potential applications about this system equivalence remain to be explored.

Although we have taken a typical family of SORs, Tannery’s pears, as an example, to study the variation of the degrees of chaos with respect to its control parameter, the model can certainly be generalized to arbitrary SORs. The parameter-dependent property of chaotic dynamics on 3D SORs enlightens an efficient and neat mechanism to control and utilize chaos, and consequently opens up many perspectives, for example, exploration and control of wave chaos in multimode fiber amplifiers to enhance pump absorption efficiency [61, 62] with nonuniform transverse, or the extensive study of a new type of microcavity [27–30]. Furthermore, exploration of chaotic dynamics within the context of non-Euclidean geometry may open a new perspective in studies of chaos in cosmology [63–65].

#### Acknowledgments

The authors thank Tsampikos Kottos from Wesleyan University for fruitful discussion on calculation of Lyapunov exponent, and Kun Tang from Bar-Ilan University for help in COMSOL simulation. C. X. acknowledges the 2019 Israeli ‘Sandwich Doctorate Program’ for international students funded by the Council for Higher Education at Bar-Ilan University. P. S. is thankful to the CNRS support under grant PICS-ALAMO. This research is also supported by The Israel Science Foundation (Grants No. 1871/15, 2074/15 and 2630/20), the United States-Israel Binational Science Foundation NSF/BSF (Grant No. 2015694), Zhejiang Provincial Natural Science Foundation of China under Grant No. LD18A040001, the National Natural Science Foundation



of China (NSFC) (grant No. 11674284 and 11974309), and National Key Research and Development Program of China (No. 2017YFA0304202).

- 
- [1] K. S. Thorne, R. H. Price, D. A. MacDonald, *Black Holes: The Membrane Paradigm* (Yale University Press, 1986).
  - [2] S. Batz, U. Peschel, Linear and nonlinear optics in curved space. *Phys. Rev. A* **78**, 043821 (2008).
  - [3] S. Batz, U. Peschel, Solitons in curved space of constant curvature. *Phys. Rev. A* **81**, 053806 (2010).
  - [4] R. Bekenstein, J. Nemirovsky, I. Kaminer, M. Segev, Shape-preserving accelerating electromagnetic wave packets in curved space. *Phys. Rev. X* **4**, 011038 (2014).
  - [5] E. Lustig *et al.*, Curved-space topological phases in photonic lattices. *Phys. Rev. A* **96**, 041804(R) (2017).
  - [6] C. Xu, A. Abbas, L. -G. Wang, S. -Y. Zhu, M. S. Zubairy, Wolf effect of partially coherent light fields in two-dimensional curved space. *Phys. Rev. A* **97**, 063827 (2018).
  - [7] C. Xu, A. Abbas, L. -G. Wang, Generalization of Wolf effect of light on arbitrary two-dimensional surface of revolution. *Opt. Express* **26**, 33263-33277 (2018).
  - [8] C. Xu, L. -G. Wang, Gouy and spatial-curvature-induced phase shifts of light in two-dimensional curved space. *New J. Phys.* **21**, 113013 (2019).
  - [9] D. Wang, C. Liu, H. Liu, J. Han, S. Zhang, Wave dynamics on toroidal surface. *Opt. Express* **26**, 17820-17829 (2018).
  - [10] H. W. Wu *et al.*, Observation of protected localized states induced by curved space in acoustic topological insulators. arXiv [Preprint] (2021). arXiv: 2101.03294 (9 January 2021).
  - [11] V. H. Schultheiss *et al.*, Optics in curved space. *Phys. Rev. Lett.* **105**, 143901 (2010).
  - [12] V. H. Schultheiss, S. Batz, U. Peschel, Hanbury Brown and Twiss measurements in curved space. *Nat. Photon.* **10**, 106-110 (2016).
  - [13] A. Patsyk, M. A. Bandres, R. Bekenstein, M. Segev, Observation of accelerating wave packets in curved space. *Phys. Rev. X* **8**, 011001 (2018).
  - [14] J. Zhu, Y. Liu, Z. Liang, T. Chen, J. Li, Elastic waves in curved space: mimicking a wormhole. *Phys. Rev. Lett.* **121**, 234301 (2018).
  - [15] R. Bekenstein *et al.*, Control of light by curved space in nanophotonic structures. *Nature Photon.* **11**, 664-670 (2017).
  - [16] Y. Song *et al.*, Möbius strip microlasers: a testbed for non-Euclidean photonics. arXiv [Preprint] (2020). arXiv: 2011.12088 (24 November 2020).
  - [17] U. Leonhardt, T. Tyc, Broadband invisibility by non-Euclidean cloaking. *Science* **323**, 110-112 (2009).
  - [18] A. Nicolet, F. Zolla, Cloaking with curved spaces. *Science* **323**, 46-47 (2009).
  - [19] L. Xu *et al.*, Light rays and waves on geodesic lenses. *Photonics Res.* **7**, 1266-1272 (2019).
  - [20] L. Xu, T. Tyc, H. Chen, Conformal Optical devices based on geodesic lenses. *Opt. Express* **27**, 28722-28733 (2019).
  - [21] G. Lefebvre *et al.*, Experiments on Maxwell's fish-eye dynamics in elastic plates. *Appl. Phys. Lett.* **106**, 024101 (2015).
  - [22] P. V. P. Cunha, C. A. R. Herdeiro, E. Radu, Fundamental photon orbits: black hole shadows and spacetime instabilities. *Phys. Rev. D* **96**, 024039 (2017).
  - [23] A. E. Motter, P. S. Letelier, FRW cosmologies between chaos and integrability. *Phys. Rev. D* **65**, 068502 (2008).
  - [24] E. Aydiner, Chaotic universe model. *Sci. Rep.* **8**, 721 (2018).
  - [25] C. Liu *et al.*, Enhanced Energy storage in chaotic optical resonators. *Nat. Photon.* **7**, 473-478 (2013).
  - [26] S. Bittner *et al.*, Suppressing spatiotemporal lasing instabilities with wave-chaotic microcavities. *Science* **361**, 1225-1231 (2018).
  - [27] C. Gmachl *et al.*, High-power directional emission from microlasers with chaotic resonators. *Science* **280**, 1556-1564 (1998).
  - [28] J. U. Nöckel, A. D. Stone, Ray and wave chaos in asymmetric resonant optical cavities. *Nature* **385**, 45-47 (1997).
  - [29] M. S. Kurdoglyan, S. -Y. Lee, S. Rim, C. -M. Kim, Unidirectional lasing from a microcavity with a rounded isosceles triangle shape. *Opt. Lett.* **29**, 2758-2760 (2004).
  - [30] J. Wiersig, M. Hentschel, Combining directional light output and ultralow loss in deformed microdisks. *Phys. Rev. Lett.* **100**, 033901 (2008).
  - [31] X. Jiang *et al.*, Chaos-assisted broadband momentum transformation in optical microresonators. *Science* **358**, 344-347 (2017).
  - [32] C. Liu *et al.*, Triggering extreme events at the nanoscale in photonic seas. *Nat. Phys.* **11**, 358-363 (2015).
  - [33] C. Liu, A. Di Falco, A. Fratalocchi, Dicke phase transition with multiple superradiant states in quantum chaotic resonators. *Phys. Rev. X* **4**, 021048 (2014).
  - [34] L. Fan, X. Yan, H. Wang, L. V. Wang, Real-time observation and control of optical chaos. *Sci. Adv.* **7**, eabc8448 (2021).
  - [35] Ya. G. Sinai, On the foundations of the ergodic hypothesis for a dynamical system of statistical mechanics. *Sov. Math. Dokl.* **4**, 1818-1822 (1963).
  - [36] M. V. Berry, Regularity and chaos in classical mechanics, illustrated by three deformations of a circular 'billiard'. *Eur. J. Phys.* **2**, 91-102 (1981).
  - [37] L. A. Bunimovich, Mushrooms and other billiards with divided phase space. *Chaos* **11**, 802-808 (2001).
  - [38] D. R. da Costa, C. P. Dettmann, E. D. Leonel, Circular, elliptic and oval billiards in a gravitational field. *Commun. Nonlinear Sci. Numer. Simulat.* **22**, 731-746 (2015).
  - [39] M. Robnik, M. V. Berry, Classical billiards in magnetic fields. *J. Phys. A: Math. Gen.* **18**, 1361-1378 (1985).
  - [40] T. Szeredi, D. A. Goodings, Classical and quantum chaos

- of the wedge billiard. I. classical mechanics. *Phys. Rev. E* **48**, 3518-3528 (1993).
- [41] Y. Kim *et al.*, Designing whispering gallery modes via transformation optics. *Nat. Photonics* **10**, 647-653 (2016).
- [42] M. Avlund, C. Ellegaard, M. Oxborrow, T. Guhr, N. Søndergaard, Observation of periodic orbits on curved two-dimensional geometries. *Phys. Rev. Lett.* **104**, 164101 (2010).
- [43] G. Tanner, N. Søndergaard, Wave chaos in acoustics and elasticity. *J. Phys. A: Math. Theor.* **40**, R443-R509 (2007).
- [44] A. N. Norri, D. A. Rebinsky, Membrane and flexural waves on thin shells. *J. Vib. Acoust.* **116**, 457-467 (1994).
- [45] D. Wang, C. Liu, S. Zhang, C. T. Chan, Chaotic photon spheres in non-Euclidean billiard. *Nanophotonics* **9**, 3367-3372 (2020).
- [46] J. B. Pendry, D. Schurig, D. R. Smith, Controlling electromagnetic fields. *Science* **312** (5781), 1780-1782 (2006).
- [47] D. Schurig, J. J. Mock, B. J. Justice, S. A. Cummer, J. B. Pendry, A. F. Starr, D. R. Smith, Metamaterial electromagnetic cloak at microwave frequencies. *Science* **314** (5801), 977-980 (2006).
- [48] The precise evolution of vector light fields is described in Section II of Ref. [2], starting from 3D Maxwell equations written in general coordinates. Specifically, for EM wave polarizing strictly along transverse direction, its wave equation also takes the form of Eq. (2), except for an extra curvature-induced potential, whose effect is discussed in Ref. [8].
- [49] U. Leonhardt, Optical conformal mapping. *Science* **312** (5781), 1777-1780 (2006).
- [50] L. Xu, H. Chen, Conformal transformation optics. *Nature Photon.* **9**, 15-23 (2015).
- [51] R. D’Inverno, *Introducing Einstein’s Relativity* (New York, Oxford University Press, 1992).
- [52] A. L. Besse, *Manifolds all of whose geodesics are closed* (Berlin-New York, Springer-Verlag, 1978).
- [53] J. E. Borzellino, C. R. Jordan-Squire, G. C. Petrics, D. M. Sullivan, On the existence of infinitely many closed geodesics on orbifolds of revolution. arXiv [Preprint] (2006). arXiv: math/0602595 (27 February 2006).
- [54] M. C. Gutzwiller, *Chaos in Classical and Quantum Mechanics* (New York, Springer-Verlag, 1990).
- [55] G. Datseris, L. Hupe, R. Fleischmann, Estimating Lyapunov exponents in billiards. *Chaos* **29**, 093115 (2019).
- [56] O. Legrand, F. Mortessagne, "Wave chaos for the Helmholtz equation" in *New Directions in Linear Acoustics and Vibration: Quantum Chaos, Random Matrix Theory and Complexity*, M. Wright, R. Weaver (Cambridge, GB. Cambridge University Press, 2010).
- [57] E. J. Heller, Bound-state eigenfunctions of classically chaotic Hamiltonian systems: scars of periodic orbits. *Phys. Rev. Lett.* **53**, 1515-1518 (1984).
- [58] Th. Zimmermann, H. -D. Meyer, H. Köppel, L. S. Cederbaum, Manifestation of classical chaos in the statistics of quantum energy levels. *Phys. Rev. A* **33**, 4334-4341 (1986).
- [59] E. B. Bogomolny, B. Georgeot, M. J. Giannoni, C. Schmit, Chaotic billiards generated by arithmetic groups. *Phys. Rev. Lett.* **69**, 1477-1480 (1992).
- [60] L. A. Bunimovich, Mechanisms of chaos in billiards: dispersing, defocusing and nothing else. *Nonlinearity* **31**, R78-R92 (2018).
- [61] L. Philippe *et al.*, Experimental study of pump power absorption along rare-earth-doped double clad optical fibres. *Opt. Commun.* **218**, 249-254 (2003).
- [62] N. A. Mortensen, Air-clad fibers: pump absorption assisted by chaotic wave dynamics? *Opt. Express* **15**, 8988-8996 (2007).
- [63] C. Ganguly, M. Bruni, Quasi-isotropic cycles and non-singular bounces in a mixmaster cosmology. *Phys. Rev. Lett.* **123**, 201301 (2019).
- [64] A. E. Motter, Relativistic chaos is coordinate invariant. *Phys. Rev. Lett.* **91**, 231101 (2003).
- [65] N. J. Cornish, E. P. S. Shellard, Chaos in quantum cosmology. *Phys. Rev. Lett.* **81**, 3571-3574 (1998).